RSC Advances

PAPER

Check for updates

Far-red-emitting double-perovskite CaLaMgSbO$_6$:Mn^{4+} phosphors with high photoluminescence efficiency and thermal stability for indoor plant cultivation LEDs

Jia Liang, Liangling Sun, Balaji Devakumar, Shaoying Wang, Qi Sun, Heng Guo, Bin Li and Xiaoyong Huang (ID) *

A series of Mn^{4+}-activated CaLaMgSbO$_6$ far-red-emitting phosphors were synthesized by a solid-state reaction route and the microstructure and optical characterizations were investigated in detail. Upon excitation at 370 and 469 nm, the samples showed intense far-red emission at about 708 nm originating from the $^2E_g \rightarrow {}^4A_{2g}$ transition and the optimal Mn^{4+} concentration was 0.7 mol%. The as-prepared phosphors also exhibited excellent internal quantum efficiency (88%) and high thermal stability. The emission intensity at room temperature dropped to 54% when the temperature rose to 423 K and the activation energy was 0.34 eV. The outstanding optical properties and the fact that the emission band of the obtained phosphors had a broad overlap with the absorption band of phytochrome P_{FR} demonstrated that the CaLaMgSbO$_6$:Mn^{4+} phosphors may be promising potential spectral converters for applying to indoor plant cultivation light-emitting diodes.

Introduction

In recent years, indoor plant growth has developed rapidly to avoid the harmful effects of extreme weather, disease, pests, and other factors on plants, which also increases the crop yield and plant quality.[1–3] The light environment is an indispensable condition for plant cultivation, and moreover, light at different wavelengths has different influences on plant growth; for example, blue light (~440 nm) can promote protein synthesis and enhance chloroplast activity, while red light (~660 nm) can accelerate the flowering and fruiting as well as increasing production,[4–11] and far-red light (~730 nm) can control the process of plant growth (adjusting the ratio of phytochrome P_{FR} and P_R to effect the growth of the plant).[12] Hence, for indoor plants, artificial light as an energy source plays an essential role. Meanwhile, it was reported that under an appropriate light-emitting diode (LED) lamp, plants grow faster than naturally grown plants because the artificial light can be adjusted according to the different light needs of the plants to achieve the most favourable conditions for plant growth.

Inorganic phosphors with admirable properties have been widely used in solid-state lighting.[13–21] Mn^{4+} as the non-rare-earth transition metal ion has the 3d^3 electron configuration and can generate deep red emissions due to the spin- and parity-forbidden $^2E_g \rightarrow {}^4A_{2g}$ transition.[22–31] Importantly, the deep red emission bands of Mn^{4+} under the excitation of near-ultraviolet (near-UV) and blue lights satisfy the demand of plant growth for far-red light. Besides, the lower price of Mn^{4+} ion also makes it an ideal activator compared with the rare-earth ions.

Recently, the double-perovskite compounds have been researched extensively due to their good chemical properties and thermal stability.[32–37] For AA′BB′O$_6$ structure compounds, B sites provide octahedral centers, in which Mn^{4+} ions can exhibit good stability and emit far-red light.[38–42] In novel double-perovskite CaLaMgSbO$_6$ (CLMS) host, Sb atoms are coordinated with 6 oxygen atoms to form [SbO$_6$] octahedrons, offering suitable sites for Mn^{4+} ions.

In this present paper, we reported double-perovskite CaLaMgSbO$_6$:Mn^{4+} (CLMS:Mn^{4+}) far-red-emitting phosphors. Under excitation by near-UV and blue lights, the as-prepared phosphors gave bright far-red emission around 708 nm, which matched well with the absorption band of phytochrome P_{FR}. Moreover, CLMS:Mn^{4+} phosphors also presented outstanding internal quantum efficiency (IQE) of 88% and good thermal stability. The above results implied that CLMS:Mn^{4+} phosphors may be promising candidates for applying to indoor plant cultivation illumination.

Experimental

Samples of CaLaMgSb$_{1-x}$O$_6$:xMn^{4+} (abbreviated as CLMS:xMn^{4+}; x = 0.1%, 0.3%, 0.5%, 0.7%, 1.0%, 1.2%, and

Key Lab of Advanced Transducers and Intelligent Control System, Ministry of Education and Shanxi Province, College of Physics and Optoelectronics, Taiyuan University of Technology, Taiyuan 030024, P. R. China. E-mail: huangxy04@126.com

1.5%) phosphors were synthesized by a conventional high-temperature solid-state reaction method in an air atmosphere. The stoichiometric amounts of raw materials $CaCO_3$ (analytical reagent, abbreviated as AR), La_2O_3 (99.99%), MgO (AR), Sb_2O_5 (AR), and $MnCO_3$ (AR) were weighed first and then ground thoroughly in an agate mortar. Subsequently, the mixtures were transferred to the alumina crucibles and then sintered at 1500 °C for 6 h in a furnace. When the samples were cooled down naturally to room temperature, ground them again for further characterizations.

The phase purity and crystal structure of the samples were recorded by an X-ray diffractometer (XRD; Bruker D8 Advance) with Cu Kα radiation. The room-temperature photoluminescence (PL) and PL excitation (PLE) spectra were measured by Edinburgh FS5 spectrometer equipped with a 150 W continuous-wave xenon lamp. The decay curves, IQE, and temperature-dependent emission spectra of the obtained phosphors were also recorded by Edinburgh FS5 spectrometer equipped with a pulsed xenon lamp, an integrating sphere coated with barium sulfate, and a temperature controller.

The as-prepared CLMS:0.7% Mn^{4+} red phosphors and silicone were mixed thoroughly to get the phosphor–silicone mixture, and then the obtained mixture was coated on the surface of the 365 nm LED chip to fabricate prototype LED device.

Results and discussion

The phase purity and structure of the as-prepared phosphors were analysed by using XRD and Rietveld refinement. Fig. 1(a) shows the XRD patterns of CLMS:xMn^{4+} (x = 0.1%, 0.7%, and 1.5%) phosphors, from which it can be seen that the main diffraction peaks of the spectra matched well with the standard card PDF#30-0261 except some small impurity peaks situated at 25.2°, 39.5°, and 52.6°, and moreover, the impurity peaks belonged to Mg_3Sb_2 (PDF#03-0375) compound, illustrating that the impurity materials were not of any manganese compound and the dopant entered into the host without significant influence. Fig. 1(b) presents the Rietveld refinement of CLMS:0.7% Mn^{4+} phosphors and Table 1 gives the relevant crystallographic parameters. The CLMS compound belonged to monoclinic $P2_1/n$ space group with lattice parameters a = 5.57801(21) Å, b = 5.65024(18) Å, c = 7.93650(30) Å, and V = 250.135(14) Å^3. In addition, with an AA′BB′O$_6$ double-perovskite structure, CLMS compound demonstrated a rock salt ordering of Mg and Sb on the B sites as displayed in Fig. 1(c).[43,44] Both Mg and Sb atoms were surrounded by 6 oxygen atoms to provide an octahedral environment for Mn. Considering the ions radius and valance state (Mg^{2+}, r = 0.72 Å, coordination number (CN) = 6; Sb^{5+}, r = 0.60 Å, CN = 6; Mn^{4+}, r = 0.53 Å, CN = 6),[45] the Mn^{4+} dopants preferred to substituted Sb^{5+} ions.
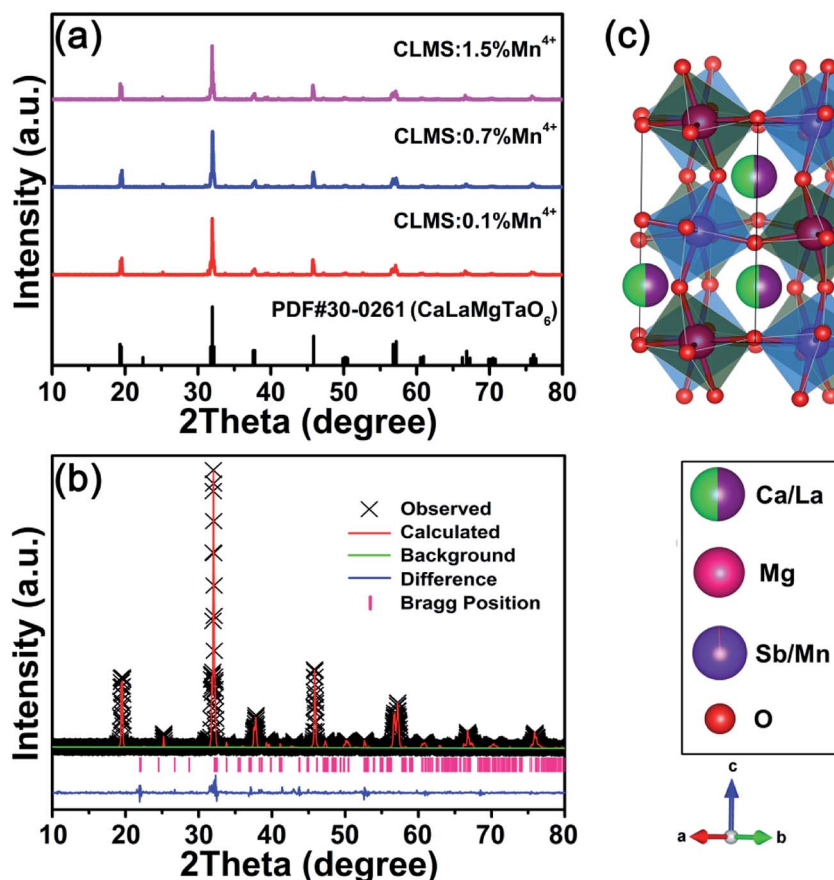

Fig. 1 (a) XRD patterns of CLMS:xMn^{4+} (x = 0.1%, 0.7%, and 1.5%) phosphors. (b and c) Rietveld refinement (b) and crystal structure (c) of CLMS:0.7% Mn^{4+} phosphors.

Table 1 Crystallographic data of CLMS:0.7% Mn^{4+} phosphors

Formula	CaLaMgSbO$_6$:0.7% Mn^{4+}
Space group	$P2_1/n$ – monoclinic
Lattice parameters	$a = 5.57801(21)$ Å
	$b = 5.65024(18)$ Å
	$c = 7.93650(30)$ Å
	$\alpha = \gamma = 90°$
	$\beta = 89.901(4)°$
Unit cell volume	$V = 250.135(14)$ Å^3

Fig. 2(a) shows the typical PLE and PL spectra of CLMS:0.7% Mn^{4+} phosphors. When monitored at 708 nm, the PLE spectrum consisted of two broad bands in the wavelength range of 250–600 nm, which matched well with the emission bands of near-UV and blue LED chips. The PLE spectrum can also be fitted by four Gaussian curves centered at 312, 371, 468, and 519 nm, which were attributed to Mn^{4+}–O^{2-} charge transfer band (CTB), $^4A_{2g} \rightarrow {}^4T_{1g}$, $^4A_{2g} \rightarrow {}^2T_{2g}$, and $^4A_{2g} \rightarrow {}^4T_{2g}$ transitions of Mn^{4+} ions, respectively.[46–48] It should be noted that the spike-like PLE peak series observed in Fig. 2(a) had been sometimes observed in some Mn^{4+}-activated fluoride phosphors that were caused by a vibronic progression of the local octahedron vibration mode or, in some cases, exogenously produced by a xenon lamp used in the PLE measurements.[49,50] It seemed that such peak series observed in the present study may be due to the xenon-lamp excitation source. Furthermore, under the excitations of 370 and 469 nm, two sharp bands at 695 and 708 nm ascribing to

the diverse vibrational modes of $^2E_g \rightarrow {}^4A_{2g}$ transitions were observed,[51,52] and the full-width at half maximum was found to be 35 nm. More importantly, the emission bands of CLMS:Mn^{4+} phosphors had a broad overlap with the absorption band of phytochrome P_{FR}, as exhibited in Fig. 2(b), which meant that CLMS:Mn^{4+} phosphors had potential application in indoor plant cultivation.

The PL spectra and relevant normalized PL intensity as a function of Mn^{4+} concentration under the 370 nm excitation were presented in Fig. 3(a). The contours of PL spectra had no change with the various concentrations of Mn^{4+} apart from the intensity. With the increasing dopant concentration, the intensity increased gradually until reached the maximum value when $x = 0.7\%$, and subsequently, the intensity decreased slowly due to the concentration quenching effect. The PLE and PL spectra of the Mn^{4+} ion clearly overlapped in the ^2E_g absorption/emission transition region.[53] However, the Mn^{4+} ion in the CLMS:Mn^{4+} phosphors acted not only as acceptor but also as donor and, therefore, no efficient radiation reabsorption occurred in these phosphors. If the acceptor and donor ions are different ions and their absorption and emission spectra efficiently overlap, then there is a risk of radiation reabsorption that often occurs in a mixture between nitride red phosphor and Y$_3$Al$_5$O$_{12}$:Ce^{3+} yellow phosphor.[54] So the energy transfer mechanism must be exchange interaction or electric multipolar interaction. According to the theory proposed by Blasse,[55] the
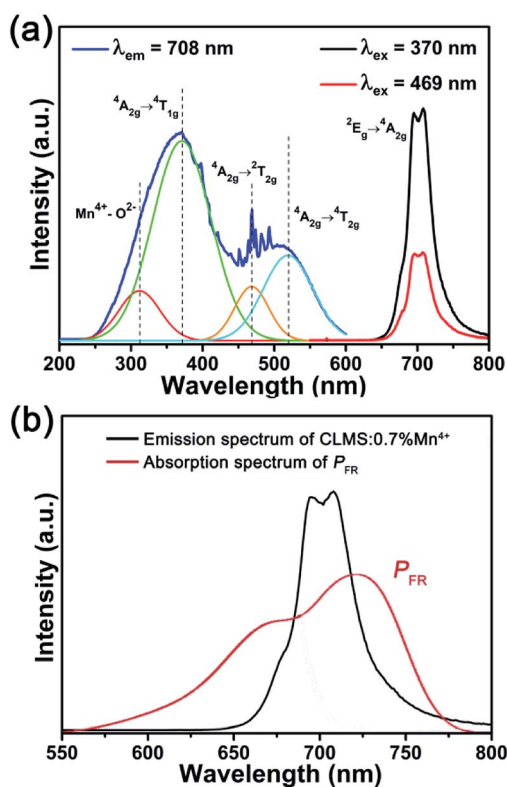

Fig. 2 (a) PLE and PL spectra of CLMS:0.7% Mn^{4+} phosphors. (b) Comparison of emission spectrum of CLMS:0.7% Mn^{4+} phosphors (λ_{ex} = 370 nm) and absorption spectrum of phytochrome P_{FR}.
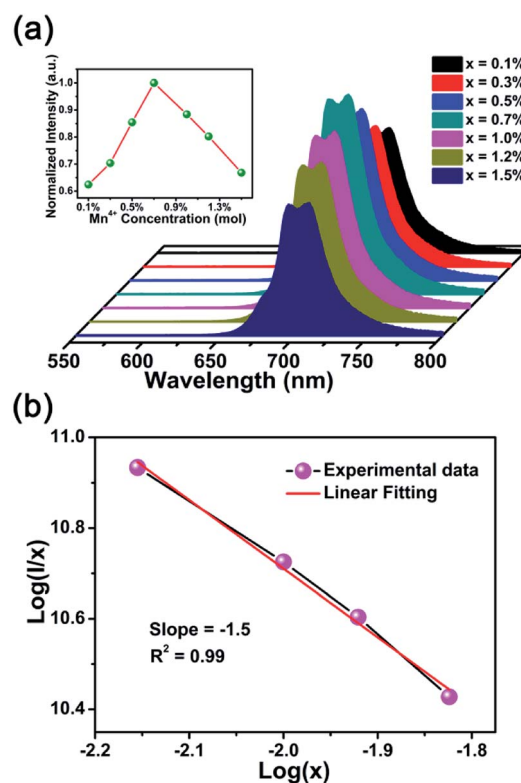

Fig. 3 (a) PL spectra of CLMS:xMn^{4+} phosphors (λ_{ex} = 370 nm). Inset shows the normalized PL intensity of CLMS:xMn^{4+} phosphors as a function of Mn^{4+} concentration. (b) Relationship between log(x) and log(I/x).

critical distance (R_c) can be used to verify the nonradiative energy transfer among the adjacent Mn^{4+} ions, as follows:[55]

$$R_c = 2\left(\frac{3V}{4\pi x_c N}\right)^{1/3} \quad (1)$$

where V is the volume of unit cell, x_c is the critical concentration of dopant ions, and N is the number of available sites for activator ions in unit cell. In this case, $V = 250.135$ Å^3, $x_c = 0.7\%$, and $N = 2$. The value of R_c was calculated to be 32.44 Å, which was far larger than 5 Å, indicating that the electric multipolar interaction triggered the concentration quenching effect. And the type of the interaction can be determined by using the equation of Dexter:[56]

$$I/x = K[1 + \beta(x)^{\theta/3}]^{-1} \quad (2)$$

where I is the emission intensity, x is the dopant concentration, K and β are the constants, and $\theta = 6$, 8, and 10 correspond to electric dipole–dipole (d–d), dipole–quadrupole (d–q), and quadrupole–quadrupole (q–q) interactions, respectively. The relationship between $\log(x)$ *vs.* $\log(I/x)$ was illustrated in Fig. 3(b), which can be well-fitted by a straight line with the slope of $\theta/3 = -1.5$. Thus, the value of θ was 4.5, manifesting that the d–d interaction dominated the concentration quenching effect in CLMS:Mn^{4+} phosphors.

The room-temperature fluorescent decay curves of CLMS:xMn^{4+} phosphors were presented in Fig. 4(a). Upon the excitation of 370 nm, the obtained decay curves can be fitted by the following double-exponential function:[57]

$$I(t) = A_1 \exp(-t/\tau_1) + A_2 \exp(-t/\tau_2) \quad (3)$$

where $I(t)$ is the PL intensity at time t; τ_1 and τ_2 refer to the short and long lifetimes for exponential components, respectively; and A_1 and A_2 are constants. Further, the effective decay process was described by the average lifetime τ_s according to the follows:[58]

$$\tau_s = (A_1\tau_1^2 + A_2\tau_2^2)/(A_1\tau_1 + A_2\tau_2) \quad (4)$$

The τ_s of CLMS:xMn^{4+} were determined to be 1.127, 1.121, 1.117, 1.113, 1.088, 1.063, and 1.039 ms corresponding to $x =$ 0.1%, 0.3%, 0.5%, 0.7%, 1.0%, 1.2%, and 1.5%, respectively. The lifetimes declined with the increasing dopant concentration, which was due to the nonradiative energy transfer among the Mn^{4+} ions.

Fig. 4(b) shows the representative CIE chromaticity diagram of CLMS:0.7% Mn^{4+} phosphors under 370 nm excitation. On the basis of the PL spectrum, the CIE coordinates were determined to be (0.7251, 0.2748), which located at far-red range. Besides, the phosphors emitted bright red light under near-UV light (inset of Fig. 4(b)). The color purity was investigated as the following equation:[59]

$$\text{Color purity} = \frac{\sqrt{(x - x_i)^2 + (y - y_i)^2}}{\sqrt{(x_d - x_i)^2 + (y_d - y_i)^2}} \times 100\% \quad (5)$$

where (x, y), (x_i, y_i), and (x_d, y_d) represent the CIE chromaticity coordinates of the sample, white illumination, and dominated wavelength, respectively. In this present work, upon excitation of 370 nm, $(x, y) = (0.7251, 0.2748)$, $(x_i, y_i) = (0.310, 0.316)$,[60] and $(x_d, y_d) = (0.7345, 0.2655)$; thus the color purity in this case was calculated to be 97.6%.

IQE is a crucial factor to evaluate the application of the phosphors.[61] The IQE of CLMS:0.7% Mn^{4+} phosphors was investigated as Fig. 4(c) according to the following formula:[62]

$$\eta_{IQE} = \frac{\int L_S}{\int E_R - \int E_S} \quad (6)$$

where L_S is the PL spectrum of the sample, E_S and E_R are the spectra of excitation light with sample and with BaSO$_4$ reference, respectively. Thus, the value of IQE reached up to 88%, which was higher than other double-perovskite phosphors, such as KMgLaTeO$_6$:Mn^{4+} (IQE: 68.9%),[63] La$_2$MgTiO$_6$:Mn^{4+} (IQE: 58.7%),[64] NaMgGdTeO$_6$:Mn^{4+} (IQE: 41.2%),[65] and NaLaMgWO$_6$:Mn^{4+} (IQE: 60%).[66]

The temperature-dependent PL spectra of CLMS:0.7% Mn^{4+} phosphors were demonstrated in Fig. 5(a). Under the excitation
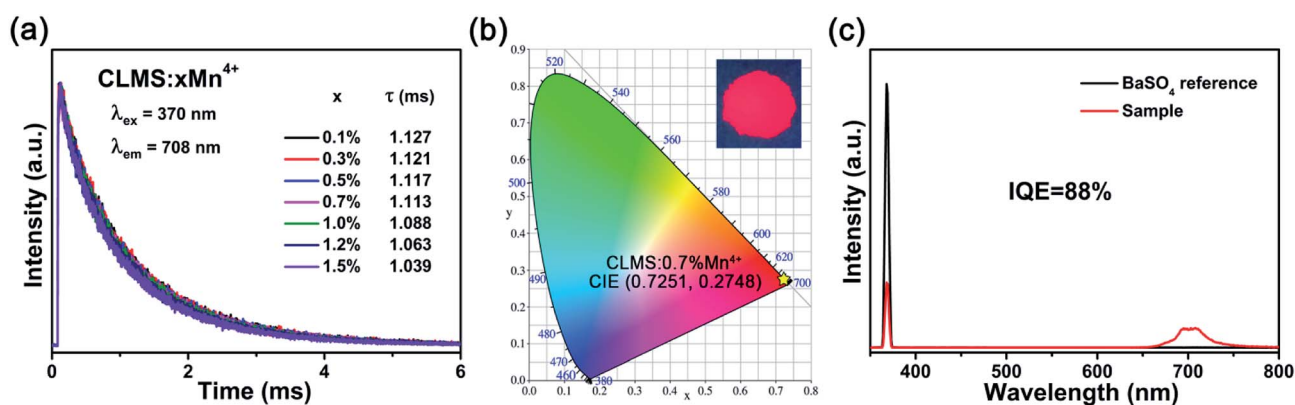

Fig. 4 (a) Decay curves of CLMS:xMn^{4+} phosphors ($\lambda_{ex} = 370$ nm; $\lambda_{em} = 708$ nm). (b) CIE chromaticity diagram of CLMS:0.7% Mn^{4+} phosphors ($\lambda_{ex} = 370$ nm). Inset shows the digital image of CLMS:0.7% Mn^{4+} phosphors under a 365 nm UV lamp. (c) The excitation line of BaSO$_4$ and the PL spectrum of CLMS:0.7% Mn^{4+} phosphors collected using an integrating sphere.
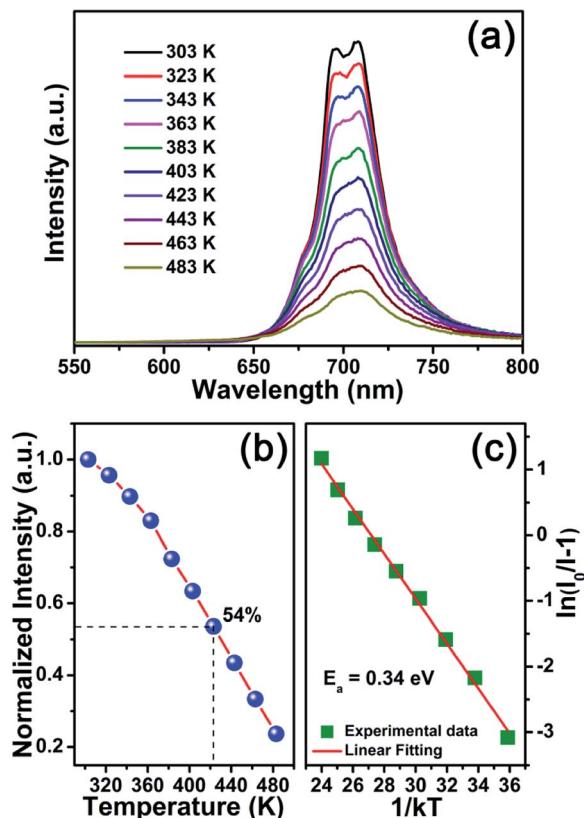
Fig. 5 (a) Temperature-dependent PL spectra of CLMS:0.7% Mn^{4+} phosphors excited at 370 nm. (b) Normalized emission intensity of CLMS:0.7% Mn^{4+} phosphors as a function of temperature. (c) Plot of ln($I_0/I - 1$) vs. $1/kT$.
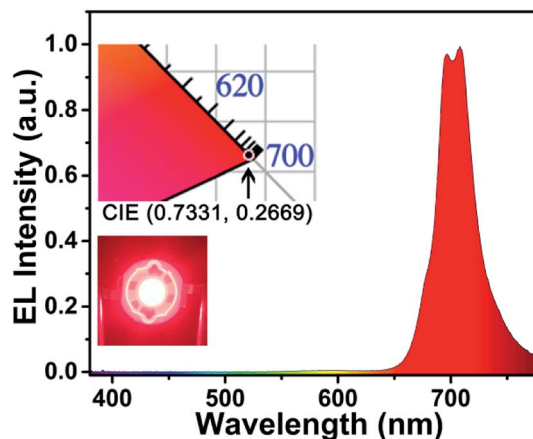

Fig. 6 EL spectrum of the fabricated far-red-emitting LED device. Insets show CIE chromaticity diagram and the luminescent image of the fabricated LED device.

of 370 nm, as the temperature was increased from 303 K to 483 K, the PL intensity decreased gradually which can be attributed to the thermal quenching effect. The PL intensity at 423 K maintained 54% of the initial value at 303 K, as shown in Fig. 5(b), which indicated an excellent thermal stability of the as-prepared phosphors. Besides, to further investigated the thermal quenching effect, the activation energy was calculated as the equation of Arrhenius:[67]

$$I(T) = \frac{I_0}{1 + c \exp(-E_a/kT)} \qquad (7)$$

where I_0 is the PL intensity in the limit of low temperatures, $I(T)$ is the PL intensity at temperature T, c is a constant, k is the Boltzmann constant, and E_a expresses the activation energy. According to the slope of the fitting line between ln($I_0/I - 1$) vs. $1/kT$ (see Fig. 5(c)), the value of E_a was obtained to be 0.34 eV. The thermal quenching effect can be explained as follows: under the excitation at 370 and 469 nm, the electrons at ground state $^4A_{2g}$ absorbed energy and transited to higher excited states $^4T_{1g}$ and $^4T_{2g}$, then relaxed to ^2E_g state through nonradiative transition. Subsequently, the excited electrons returned to $^4A_{2g}$ state with characteristic far-red light.[68] When at high temperature environment, a part of excited electrons absorbed activation energy and jumped to the cross-point between ground state and excited states. Finally, these

excited electrons went back to the ground state without giving rise to fluorescence, and such process increased the probability of nonradiative transition and resulted in the thermal quenching phenomenon. So the high activation energy meant a good thermal stability. For CLMS:0.7% Mn^{4+} phosphors, the activation energy was determined to be 0.34 eV, which was slightly smaller than those reported for other Mn^{4+}-activated oxide phosphors ($\sim$0.55–0.75 eV),[50] but was considerably larger than the value of $\sim$0.14 eV for Y$_3$Al$_5$O$_{12}$ (YAG):Ce^{3+}.[69] Thus, the CLMS:Mn^{4+} phosphors were understood to be highly thermal stable.

In order to test the effect of the as-prepared phosphors in practical applications, a prototype far-red LED device was fabricated with the help of CLMS:0.7% Mn^{4+} phosphors and a 365 nm LED chip. The electroluminescence (EL) spectrum presented an intense far-red emission band ranging from 650 to 800 nm, which corresponding to the PL spectra of the phosphors as shown in Fig. 6. From the inset, bright red light was observed from the LED device under 60 mA current and 3 V voltage, and the CIE coordinates were obtained to be (0.7331, 0.2669), matching well with the need of the plant growth for deep red light. The above results demonstrated that the CLMS:Mn^{4+} far-red phosphors were potential materials for applying in indoor plant growth.

Conclusions

Novel Mn^{4+}-activated CaLaMgSbO$_6$ far-red-emitting phosphors were synthesized via a high-temperature solid-state reaction method. The phosphors exhibited intense far-red light centered at about 708 nm when excited at 370 and 469 nm. The optimal concentration of Mn^{4+} ions was 0.7 mol%, and the CIE chromaticity coordinates of CLMS:0.7% Mn^{4+} sample were (0.7251, 0.2748) which situated at far red region. The phosphors had high IQE of 88%, and also showed excellent thermal stability that the PL intensity at 423 K was 54% of that at 303 K. The above splendid luminescence properties illustrated that the

CLMS:Mn^{4+} compounds were potential far-red-emitting phosphors for plant cultivation LEDs applications.

Conflicts of interest

There are no conflicts to declare.

Acknowledgements

Notes and references

1 N. Yeh and J.-P. Chung, *Renewable Sustainable Energy Rev.*, 2009, **13**, 2175–2180.

2 X. Huang and H. Guo, *Dyes Pigm.*, 2018, **152**, 36–42.

3 T. Nakajima and T. Tsuchiya, *ACS Appl. Mater. Interfaces*, 2015, **7**, 21398–21407.

4 J. Chen, N. Zhang, C. Guo, F. Pan, X. Zhou, H. Suo, X. Zhao and E. M. Goldys, *ACS Appl. Mater. Interfaces*, 2016, **8**, 20856–20864.

5 P. F. Devlin, J. M. Christie and M. J. Terry, *J. Exp. Bot.*, 2007, **58**, 3071–3077.

6 R. Cao, Z. Shi, G. Quan, T. Chen, S. Guo, Z. Hu and P. Liu, *J. Lumin.*, 2017, **188**, 577–581.

7 Z. Zhou, J. Zheng, R. Shi, N. Zhang, J. Chen, R. Zhang, H. Suo, E. M. Goldys and C. Guo, *ACS Appl. Mater. Interfaces*, 2017, **9**, 6177–6185.

8 Y. J. Yun, J. K. Kim, J. Y. Ju, S. K. Choi, W. I. Park, J. Y. Suh, H. K. Jung, Y. Kim and S. Choi, *Phys. Chem. Chem. Phys.*, 2017, **19**, 11111–11119.

9 N. Yeh, T. J. Ding and P. Yeh, *Renewable Sustainable Energy Rev.*, 2015, **51**, 55–61.

10 Y. Zheng, H. Zhang, H. Zhang, Z. Xia, Y. Liu, M. S. Molokeev and B. Lei, *J. Mater. Chem. C*, 2018, **6**, 4217–4224.

11 Z. Zhou, M. Xia, Y. Zhong, S. Gai, S. Huang, Y. Tian, X. Lu and N. Zhou, *J. Mater. Chem. C*, 2017, **5**, 8201–8210.

12 K. A. Franklin and P. H. Quail, *J. Exp. Bot.*, 2010, **61**, 11–24.

13 J. Xue, X. Wang, J. H. Jeong and X. Yan, *Phys. Chem. Chem. Phys.*, 2018, **20**, 11516–11541.

14 X. Li, D. Xu, X. Liu and H. Guo, *RSC Adv.*, 2017, **7**, 53839–53845.

15 D. Chen, S. Yuan, X. Li and W. Xu, *RSC Adv.*, 2017, **7**, 36168–36174.

16 J. Qiao, L. Ning, M. Molokeev, Y.-C. Chuang, Q. Liu and Z. Xia, *J. Am. Ceram. Soc.*, 2018, **140**, 9730–9736.

17 X. Huang, *Nat. Photonics*, 2014, **8**, 748–749.

18 Y. Zhu, L. Cao, M. G. Brik, X. Zhang, L. Huang, T. Xuan and J. Wang, *J. Mater. Chem. C*, 2017, **5**, 6420–6426.

19 X. Huang, *J. Alloys Compd.*, 2017, **690**, 356–359.

20 B. Li, X. Huang, H. Guo and Y. Zeng, *Dyes Pigm.*, 2018, **150**, 67–72.

21 P. Du, L. Luo, X. Huang and J. S. Yu, *J. Colloid Interface Sci.*, 2018, **514**, 172–181.

22 Q. Sun, S. Wang, B. Li, H. Guo and X. Huang, *J. Lumin.*, 2018, **203**, 371–375.

23 P. Cai, X. Wang and H. J. Seo, *Phys. Chem. Chem. Phys.*, 2018, **20**, 2028–2035.

24 D. Chen, Y. Zhou and J. Zhong, *RSC Adv.*, 2016, **6**, 86285–86296.

25 Q. Sun, B. Li, S. Wang, H. Guo and X. Huang, *J. Mater. Sci.: Mater. Electron.*, 2018, **29**, 12972–12977.

26 S. Liang, M. Shang, H. Lian, K. Li, Y. Zhang and J. Lin, *J. Mater. Chem. C*, 2017, **5**, 2927–2935.

27 M. Zhu, Y. Pan, L. Xi, H. Lian and J. Lin, *J. Mater. Chem. C*, 2017, **5**, 10241–10250.

28 L. Xi, Y. Pan, M. Zhu, H. Lian and J. Lin, *J. Mater. Chem. C*, 2017, **5**, 9255–9263.

29 S. Wang, Q. Sun, B. Devakumar, L. Sun, J. Liang and X. Huang, *RSC Adv.*, 2018, **8**, 30191–30200.

30 K. Sankarasubramanian, B. Devakumar, G. Annadurai, L. Sun, Y.-J. Zeng and X. Huang, *RSC Adv.*, 2018, **8**, 30223–30229.

31 M. Peng, X. Yin, P. A. Tanner, M. G. Brik and P. Li, *Chem. Mater.*, 2015, **27**, 2938–2945.

32 J. Liang, L. Sun, B. Devakumar, S. Wang, Q. Sun, H. Guo, B. Li and X. Huang, *RSC Adv.*, 2018, **8**, 27144–27151.

33 Q. Liu, L. Wang, W. Huang, L. Zhang, M. Yu and Q. Zhang, *J. Alloys Compd.*, 2017, **717**, 156–163.

34 R. Yu, C. Wang, J. Chen, Y. Wu, H. Li and H. Ma, *ECS J. Solid State Sci. Technol.*, 2014, **3**, R33–R37.

35 T. T. Deng, E. H. Song, Y. Y. Zhou, L. Y. Wang and Q. Y. Zhang, *J. Mater. Chem. C*, 2017, **5**, 12422–12429.

36 Y. Liang, H. M. Noh, W. Ran, S. H. Park, B. C. Choi, J. H. Jeong and K. H. Kim, *J. Alloys Compd.*, 2017, **716**, 56–64.

37 J. Zhong, D. Chen, X. Chen, K. Wang, X. Li, Y. Zhu and Z. Ji, *Dalton Trans.*, 2018, **47**, 6528–6537.

38 D. R. Kim, S. W. Park, B. K. Moon, S. H. Park, J. H. Jeong, H. Choi and J. H. Kim, *RSC Adv.*, 2017, **7**, 1464–1470.

39 P. Cai, L. Qin, C. Chen, J. Wang, S. Bi, S. I. Kim, Y. Huang and H. J. Seo, *Inorg. Chem.*, 2018, **57**, 3073–3081.

40 G. Jiang, B. Yang, G. Zhao, Y. Liu, J. Zou, H. Sun, H. Ou, Y. Fang and J. Hou, *Opt. Mater.*, 2018, **83**, 93–98.

41 H. Chen, H. Lin, Q. Huang, F. Huang, J. Xu, B. Wang, Z. Lin, J. Zhou and Y. Wang, *J. Mater. Chem. C*, 2016, **4**, 2374–2381.

42 Y. Li, S. Qi, P. Li and Z. Wang, *RSC Adv.*, 2017, **7**, 38318–38334.

43 L. Wang, Q. Liu, K. Shen, Q. Zhang, L. Zhang, B. Song and C. Wong, *J. Alloys Compd.*, 2017, **696**, 443–449.

44 Q. Liu, L. Wang, W. Huang, X. Li, M. Yu and Q. Zhang, *Ceram. Int.*, 2017, **43**, 16292–16299.

45 Q. Liu, L. Wang, W. Huang, X. Li, M. Yu and Q. Zhang, *Ceram. Int.*, 2018, **44**, 1662–1667.

46 A. Fu, L. Zhou, S. Wang and Y. Li, *Dyes Pigm.*, 2018, **148**, 9–15.

47 Q. Huang, W. Ye, G. Hu, X. Jiao and X. Liu, *J. Lumin.*, 2018, **194**, 557–564.

48 J. Y. Park, J. S. Joo, H. K. Yang and M. Kwak, *J. Alloys Compd.*, 2017, **714**, 390–396.

49 S. Adachi, *J. Lumin.*, 2018, **197**, 119–130.

50 S. Adachi, *J. Lumin.*, 2018, **202**, 263–281.

51 Y. Xu, Y. Zhang, L. Wang, M. Shi, L. Liu and Y. Chen, *J. Mater. Sci.: Mater. Electron.*, 2017, **28**, 12032–12038.

52 J. Long, X. Yuan, C. Ma, M. Du, X. Ma, Z. Wen, R. Ma, Y. Wang and Y. Cao, *RSC Adv.*, 2018, **8**, 1469–1476.

53 T. Arai and S. Adachi, *Jpn. J. Appl. Phys.*, 2011, **50**, 092401.

54 B. Wang, H. Lin, J. Xu, H. Chen and Y. Wang, *ACS Appl. Mater. Interfaces*, 2014, **6**, 22905–22913.

55 G. Blasse, *Phys. Lett. A*, 1968, **28**, 444–445.

56 D. L. Dexter, *J. Chem. Phys.*, 1953, **21**, 836–850.

57 X. Huang, B. Li and H. Guo, *J. Alloys Compd.*, 2017, **695**, 2773–2780.

58 P. Du, X. Huang and J. S. Yu, *Inorg. Chem. Front.*, 2017, **4**, 1987–1995.

59 X. Huang, B. Li, H. Guo and D. Chen, *Dyes Pigm.*, 2017, **143**, 86–94.

60 H. Guo, X. Huang and Y. Zeng, *J. Alloys Compd.*, 2018, **741**, 300–306.

61 X. Huang, H. Guo and B. Li, *J. Alloys Compd.*, 2017, **720**, 29–38.

62 P. Du, X. Huang and J. S. Yu, *Chem. Eng. J.*, 2018, **337**, 91–100.

63 K. Li, H. Lian and R. Van Deun, *Dalton Trans.*, 2018, **47**, 2501–2505.

64 Y. Takeda, H. Kato, M. Kobayashi, H. Kobayashi and M. Kakihana, *Chem. Lett.*, 2015, **44**, 1541–1543.

65 K. Li, H. Lian and D. R. Van, *J. Lumin.*, 2018, **198**, 155–162.

66 X. Huang, J. Liang, B. Li, L. Sun and J. Lin, *Opt. Lett.*, 2018, **43**, 3305–3308.

67 S. A. Arrhenius, *Z. Phys. Chem.*, 1889, **4**, 96–116.

68 S. Zhang, Y. Hu, H. Duan, Y. Fu and M. He, *J. Alloys Compd.*, 2016, **693**, 315–325.

69 Y. Zhang, L. Li, X. Zhang and Q. Xi, *J. Rare Earths*, 2008, **26**, 446–449.